

# Predissociation dynamics of $I_2(B)$ in liquid $CCl_4$ observed through femtosecond pump-probe measurements: Electronic caging through solvent symmetry

R. Zadoyan, M. Sterling, M. Ovchinnikov, and V. A. Apkarian  
*Department of Chemistry, University of California, Irvine, California 92697-2025*

(Received 4 April 1997; accepted 18 August 1997)

Direct observations of the solvent induced electronic predissociation of  $I_2(B)$  in liquid  $CCl_4$  are made using femtosecond pump-probe measurements in which fluorescence from spin-orbit excited  $I^*I^*$  pairs, bound by the solvent cage, is used as detection. Data is reported for initial preparations ranging from the  $B$  state potential minimum, at 640 nm, to above the dissociation limit, at 490 nm. Analysis is provided through classical simulations, to highlight the role of solvent structure on: recombination, vibrational relaxation, and decay of coherence. The data is consistent with an anisotropic  $I_2(X)-CCl_4$  potential which, in the first solvent shell, leads to an angular distribution peaked along the molecular axis. The roles of solvent structure and dynamics on electronic predissociation are analyzed. The data in liquid  $CCl_4$  can be understood in terms of a curve crossing near  $v=0$ , at  $3.05 \text{ \AA} < R_c < 3.8 \text{ \AA}$ , and the final surface can be narrowed down to  $2_g$  or  $a(1_g)$ . This nonadiabatic  $u \rightarrow g$  transition is driven by static and dynamic asymmetry in the solvent structure. The role of solvent structure is demonstrated by contrasting the liquid phase predissociation probabilities with those observed in solid Kr. Despite the twofold increase in density, predissociation probabilities in the solid state are an order of magnitude smaller, due mainly to the high symmetry of the solvent cage. The role of solvent dynamics is evidenced in the energy dependent measurements. Independent of the kinetic energy content in  $I_2$ , electronic predissociation in liquid  $CCl_4$  proceeds with a time constant equal to the molecular vibrational period. A modified Landau-Zener model, in which the effective electronic coupling is taken to be a linear function of vibrational amplitude fits the data, and suggests that cage distortions driven by the molecule enhance its predissociation probability. A nearly quantitative reproduction of the observations is possible when using the recently reported off-diagonal DIM surface that couples the  $B(0_u^+)$  and  $a(1_g)$  states [Batista and Coker, *J. Chem. Phys.* **105**, 4033 (1996)]. © 1997 American Institute of Physics. [S0021-9606(97)00544-8]

## I. INTRODUCTION

Ever since the first experimental studies of Eisenthal *et al.*,<sup>1</sup> the solvent induced predissociation of the  $B(^3\Pi_{0u}^+)$  electronic state of molecular iodine has become a prototype for investigating nonadiabatic dynamics in condensed media. The literature on this subject is extensive. Here we cite a select set of recent developments, noting that extensive citations of the relevant literature are given in these references.<sup>2-12</sup> With the combination of ultrafast experimentation, and nearly exact numerical methods for treating nonadiabatic many-body dynamics,<sup>9,11,12</sup> an accurate description of the coupled electronic-nuclear dynamics in this model system including all electronic states, now seems a realistic goal.

The picosecond era of measurements in the liquid phase,<sup>2</sup> mostly through transient absorption measurements, concluded that the predissociation of  $I_2(B)$  occurs on a time scale shorter than 1 ps.<sup>3,4</sup> The fact that electronic predissociation proceeds on a time scale comparable to vibrational periods, immediately raises doubts about the notion of describing the underlying dynamics as a rate process, and its characterization by a single decay constant.

With a time resolution of 30 fs, Scherer *et al.* studied the

predissociation dynamics of  $I_2(B)$  in the liquid phase through careful measurements and analysis of transient dichroism and birefringence.<sup>5</sup> They prepared the excited state using short pulses at 580 nm, and monitored the time evolution of the prepared coherence with variable wavelengths. They concluded that the decay time of the prepared coherence of 230 fs was controlled by predissociation, confirming a time scale shorter than the equilibration of nuclear coordinates. Moreover, based on probe wavelength dependence of the appearance time of the transient, among the several possible curve crossings<sup>13</sup> (see Fig. 1), they concluded that the likely candidate for the main predissociation channel was the  $a(1_g)$  surface.<sup>5</sup>

With the advantage of structural order, measurements of the same process in the solid state could provide an additional tool for characterizing this solvent induced intramolecular electron transfer. We reported such studies performed in solid Kr, in which we used femtosecond pump-probe spectroscopy relying on fluorescence from the molecular ion-pair states.<sup>6</sup> We showed that for very similar initial preparations of the molecule, the solid state predissociation probabilities were nearly an order of magnitude smaller than what had been observed in the liquid phase.<sup>6</sup> Given the nearly twofold increase in local density, an order of magnitude re-

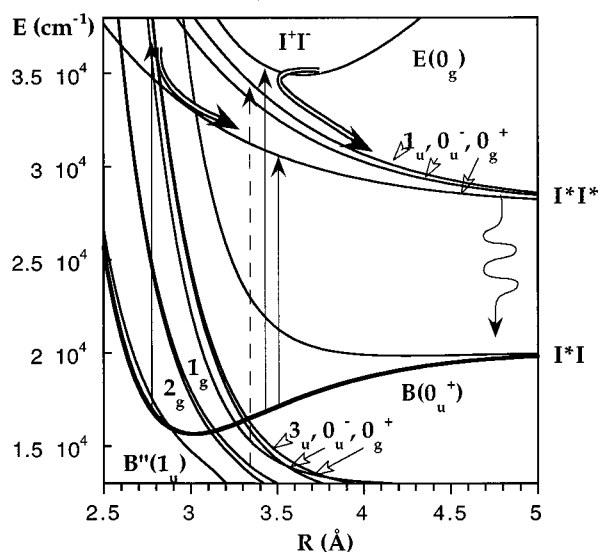


FIG. 1. Relevant potential curves. The pump-probe experiments prepare the  $B$  state, and interrogate the time dependent populations by a variety of dipole allowed transitions, as indicated by the up-arrows. Fluorescence from  $I^*I^* \rightarrow I^*I$  is used as detection, with a variety of direct and indirect channels leading to the population of the upper state. The indicated curves that cross the  $B$  state were taken from Ref. 13.

duction in curve crossing probabilities is not a trivially obvious result. A more direct comparison of observables, using the same experimental technique, seemed warranted. In this paper we report single color pump-probe studies in liquid  $CCl_4$ , with initial preparation that spans the full range of the molecular potential, from minimum to above dissociation limit. Our liquid phase measurements are in agreement with those of Scherer *et al.* Indeed predissociation in the solid state is slower than in the liquid state. We will argue that this result can be understood in terms of the local solvent structure. After narrowing down the main predissociation channel to  $a(1_g)$  or  $2_g$  surfaces, we recognize that the requisite dipolar character of the off-diagonal surface that couples these states undergoes severe cancellation when the local solvent structure is highly symmetric. The electronic curve crossing is induced by static and dynamic solvent asymmetry, a collective effect which does not simply scale with solvent density.

Quite relevant to the condensed phase studies are the high pressure gas phase measurements of Zewail *et al.*,<sup>7,8</sup> who in their most recent work show a strongly nonlinear density dependence of  $T_2$  and  $T_1$  times, where  $T_1$  can be identified with the predissociation of  $I_2(B)$ .<sup>8</sup> These experiments help identify the nature of the off-diagonal matrix elements that lead to predissociation. Both long range and short range interactions are implicated.

On the theoretical front, we mention three important developments. In an ambitious undertaking, Batista and Coker (BC), have presented simulations of  $I_2$  first in liquid Xe,<sup>9(a)</sup> and more recently in solid Ar and Xe,<sup>9(b)</sup> in which nonadiabatic transitions among all 23 states that correlate with the ground  $I(^2P) + I(^2P)$  have been included. They construct a semiempirical diatomics-in-molecules (DIM) Hamiltonian

matrix for the  $I_2$ -Rg interactions, and propagate trajectories on the coupled electronic surfaces. A DIM Hamiltonian for  $I_2$ -Ar was also constructed by Buchachenko and Stepanov, who dissected the  $I_2$ -Ar surfaces and off-diagonal couplings involving the  $B$  state.<sup>10</sup> The reported simulations with the DIM potentials lead to extremely rapid predissociation, through a variety of crossings, in qualitative agreement with the liquid phase results. However, the solid Ar simulations also predict ultrafast predissociation, now in discord with experiment. It would seem that adjustment of the elements in the DIM Hamiltonian are necessary, and at present, experiments are the only viable means to this end.

Ben-Nun and Levine considered the liquid phase predissociation of  $I_2$  through simulations that carefully treat the nuclear nonadiabatic dynamics, while assuming a simplified electrostatic model for the electronic coupling between states.<sup>11</sup> Their treatment is limited to the consideration of the crossing between  $B(0_u^+)$  and  $a(1_g)$  curves, and designed to be in agreement with the experiments of Scherer *et al.*<sup>5</sup> They underscore the strong local density dependence of rates in their model, which would suggest that predissociation in the solid state would be significantly faster than in the liquid phase. A more careful treatment of the electrostatic coupling was provided by Roncero, Halberstadt, and Beswick, (RHB), in their treatment of the predissociation of the  $I_2$ -Ar van der Waals complex, in which they explicitly indicated the angular anisotropy of the coupling surface.<sup>12</sup> As we elaborate, this is implicit in the DIM treatment,<sup>9,10</sup> and key to understanding predissociation in dense media.

The usual femtosecond pump-probe measurements on  $I_2$  use the molecular ion-pair states as the terminus for the probe transition.<sup>14</sup> Such measurements have not been possible in the liquid phase, due to rapid quenching of the ion-pair states in such media. To overcome this difficulty our experiments were designed to use the  $I^*I^*$  surfaces as final states. All three states that arise from  $I^*(^2P_{1/2}) + I^*(^2P_{1/2})$  are repulsive (see Fig. 1) and do not sustain population in the gas phase.<sup>15</sup> However, in condensed media, the pair of spin-excited atoms can remain in contact per force of the solvent cage, with radiation as their main relaxation channel. A detailed spectroscopic analysis of these transitions, and the photodynamics of the doubly spin-excited  $I^*I^*$  states in various liquids and solid matrices, has already been given.<sup>16</sup> In the time resolved studies we report here, we use the  $I^*I^* \rightarrow I^*I$  emission as detection. Note, in principle both  $B(0_u^+)$  and  $a(1_g)$  states can be probed via  $I^*I^*(0_g^+) \leftarrow I^*I(B(0_u^+))$  and  $I^*I^*(1_u) \leftarrow I_2(a(1_g))$  transitions, as indicated in Fig. 1. However, the strong  $E \leftarrow B$  transition, masks the absorption from the  $a(1_g)$  state, precluding direct experimental information about its role.

We follow the format of dynamical spectroscopy as previously outlined.<sup>6</sup> The experimental observables, consisting of time dependent resonances, are analyzed with the help of classical simulations. The methods of experiment and simulation are presented in Secs. II and III, respectively. The experimental observations are summarized in Sec. IV, and analyzed in Sec. V. In Sec. VI we discuss the implications

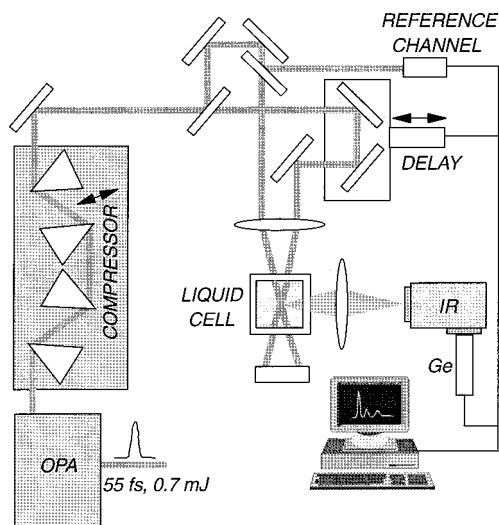


FIG. 2. Experimental layout.

with a critical evaluation of theories. Concluding remarks are provided in Sec. VII.

## II. EXPERIMENT

The experimental setup is illustrated in Fig. 2. The measurements are conducted in a two-window quartz cell containing a static solution of  $I_2$  in liquid  $CCl_4$ . The concentration of the solution is adjusted to an optical density of  $\sim 1$  at 520 nm. The data are quite insensitive to concentration.

The laser source consists of a femtosecond Ti:Sapphire oscillator, the 800 nm output of which is stretched, regeneratively amplified and recompressed to 55 fs at a repetition rate of 1 kHz (0.7 mJ/pulse). The amplified output is then used to pump a BBO based three stage optical parametric amplifier with 20% conversion efficiency. The OPA output is up-converted using a 0.5 mm thick BBO crystal, either by doubling or by summing with the 800 nm fundamental. This allows a coverage of the spectral range between 480 and 800 nm. A prism compressor, with a limiting diaphragm before the folding mirror, is used to maintain near transform limited pulses throughout the tuning range of the OPA with typical pulse widths of 50–65 fs. The compressor is adjusted to compensate for group velocity dispersion (GVD) introduced by optical elements in the beam path before it reaches the sample. The compressed, up-converted output of the OPA is split evenly with a 50% beam splitter in a Michelson-type interferometer. After passing through a variable delay line, using a single lens ( $f_l = 20$  cm), the two beams are recombined at an angle of  $5^\circ$  immediately behind the entrance window of the cell. The noncollinear geometry of the experiment avoids interferometric noise in these single color experiments at the expense of sacrificing time resolution. At  $5^\circ$  of recombination angle, with a beam waist of 0.1 mm at the crossing point, the time resolution broadens by  $\sim 10\%$ . The experimental time resolution is verified for each wavelength by measuring the autocorrelation trace when the liquid cell is

replaced with a 0.2 mm thick BBO crystal. The intensities of both beams are attenuated by a factor of  $\sim 2$  below the white light generation limit in the cell.

Infrared fluorescence from the beam overlap region is collected at right angle, with a single lens, through a 0.25 m monochromator, and detected with a liquid nitrogen cooled Ge detector (response time =  $0.5 \mu s$ ). The detector output is amplified and integrated with a boxcar while simultaneously monitoring the OPA output through a second channel of the boxcar integrator. Data is collected when the reference signal falls within a 2% window of a preset level. Typically, at each delay, 1000 selected pulses are acquired and averaged in a computer.

The experiments to be reported consist of single color pump-probe measurements. Accordingly, the transients should in principle be strictly symmetric in time. A systematic linear deviation from such a symmetry, of  $\sim 50$  fs over a scan of 1 ps is observed experimentally. Using interference fringes from a He:Ne laser we have verified that this is not the result of nonlinearity in the mechanical drive, and ascribe it to a combination of beam walk-off in the unconstrained volume of the solution, and spatial chirp in the pulses. Although the effect is noticeable, we do not correct the data for this systematic error.

## III. SIMULATIONS

The classical molecular dynamics simulations used in the interpretation of the data to be presented are carried out by standard methods. A cell of 108 particles subject to periodic boundary conditions is considered, and the equations of motion for the microcanonical ensemble are propagated using the Verlet algorithm. With the pair potentials defined, the cell dimensions are adjusted such that the pressure of the simulated system fluctuates about  $P=0$ , while the temperature fluctuates about  $T=300$  K. This corresponds to a reduced density of  $\rho^* = 0.7$  in the present simulation of  $CCl_4$  under room temperature and pressure conditions. The  $CCl_4$  molecules are represented by single particles with pairwise additive Lennard-Jones intermolecular potentials,<sup>17</sup> for parameters see Table I. Two different potential constructs are used to describe the  $I_2-CCl_4$  interaction in the ground  $X(^1\Sigma_g^+)$  state of the molecule. The first, to which we refer as isotropic potentials, consists of pairwise additive atom-atom potentials, in which the  $I-CCl_4$  potential is treated as Lennard-Jones, with parameters suitable for  $Xe-CCl_4$  interaction (see Table I). The second, to which we refer as anisotropic potentials, is a three body potential constructed as

$$V(I_2(X)-CCl_4) = \sum_{i=1,2} \cos^2(\theta_i) V_{\Sigma}(r_i) + \sin^2(\theta_i) V_{\Pi}(r_i) \quad (1)$$

in which the indices 1 and 2 refer to the I atoms,  $\theta$  is measured from the I-I axis,  $V_{\Sigma}$  and  $V_{\Pi}$  are expressed as Morse functions, derived from known I-Rg potentials,<sup>18</sup> and scaled by the rules appropriate for nonbonded interactions

TABLE I. Potential parameters used in simulations.

Lennard-Jones: $V = 4 \epsilon [(\sigma/r)^{12} - (\sigma/r)^6]$			
	$\sigma(\text{\AA})$	$\epsilon(\text{cm}^{-1})$	
CCl <sub>4</sub> -CCl <sub>4</sub>	5.881	227	
I(B)-CCl <sub>4</sub> (Xe-CCl <sub>4</sub> )	4.968	190	
Xe-Xe	4.055	159	
Morse: $V = D_e [1 - \exp(-\beta(r-r_e))]^2$			
	$D_e(\text{cm}^{-1})$	$r_e(\text{\AA})$	$\beta(\text{\AA}^{-1})$
V <sub>Σ</sub> (I-CCl <sub>4</sub> )	336	4.96	1.12
V <sub>Π</sub> (I-CCl <sub>4</sub> )	147.5	5.71	1.16
I <sub>2</sub> (B)	4503.6	3.016	1.85
I* <sub>1</sub> (1g)	240	6.2	0.46
Exponential: $V = C_1 + C_2 \exp(-r/C_3)$			
	$C_1(\text{cm}^{-1})$	$C_2(\text{cm}^{-1})$	$C_3(\text{\AA})$
I <sub>2</sub> (a)	11928	6.34 × 10 <sup>7</sup>	0.33

$$D_e(\text{I-CCl}_4) = \sqrt{\frac{\epsilon_{\text{CCl}_4}}{\epsilon_{\text{Rg}}}} D_e(\text{I-Rg}), \quad (2a)$$

$$r_e(\text{I-CCl}_4) = \frac{\sigma_{\text{CCl}_4}}{\sigma_{\text{Rg}}} r_e(\text{I-Rg}), \quad (2b)$$

$$\beta(\text{I-CCl}_4) = \frac{\sigma_{\text{Rg}}}{\sigma_{\text{CCl}_4}} \beta(\text{I-Rg}), \quad (2c)$$

in which  $D_e$ ,  $r_e$ , and  $\beta$  are the Morse parameters, and  $\sigma$  and  $\epsilon$  are the Lennard-Jones parameters for Rg-Rg and CCl<sub>4</sub>-CCl<sub>4</sub> interactions. Note, in the form given in Eq. (1),  $V_{\Sigma}$  is responsible for the linear well on the I-I-CCl<sub>4</sub> surface. It can be shown, quite generally for rare gas-molecular halogen interactions, that the linear well arises from the admixture of ionic character in the ground surface.<sup>19</sup> Accordingly, in polarizable media in which the ionic excited states are strongly solvated, it can be expected that the linear minima will be even deeper. The ground state potential determines structure of the solvent from where the excitation is initiated, and will accordingly effect coherences, recombination and energy dissipation. In the excited  $B(^3\Pi_{0u}^+)$  state, the I-CCl<sub>4</sub> potentials are treated as isotropic. The justification for using an anisotropic ground state and isotropic excited state atom-atom potentials has been given before.<sup>19-21</sup>

The simulations are started by Monte Carlo sampling of initial conditions from a file thermalized on the ground state. The excited state potentials are then used to propagate the equations of motion. In accord with the Franck-Condon principle for vertical excitations, the initial I-I coordinate distribution is chosen to match the reflection of the laser spectral distribution from the difference potential of the transition.<sup>22</sup> The pump-probe signal can then be generated from an ensemble of  $N$  trajectories by temporal and spectral convolution of the probe laser with the many-body difference potential

$$S(t) = \frac{1}{N} \sum_{i=1}^N \int_{-\infty}^{+\infty} dt' \int_{-\infty}^{\infty} dh \nu |\mu_{nm}(\{R_k\})|^2 \times W(h\nu_{\text{probe}}, t'; t) \delta[\Delta V_{nm}(\{R_k\}, t) - h\nu] \quad (3)$$

in which the indices  $n$  and  $m$  refer to the initial and final electronic states of the probe transition, and at a time delay  $t$  between pump and probe pulses, the probe laser intensity is characterized spectrally and temporally by the window function,  $W(h\nu_{\text{probe}}, t)$ .<sup>22</sup> In practice, since the many-body electronic surfaces are not known *a priori*, the interpretation of observed transients is greatly simplified by an effective one-dimensional inversion of the trajectory data, under the assumption that the probe difference potential is mainly governed by the I-I coordinate,  $R$ . For a fixed probe resonance, this also allows the neglect of the coordinate dependent transition dipole. Thus

$$\begin{aligned} S(t) &= \frac{1}{N} \sum_{i=1}^N \int_{-\infty}^{+\infty} dt' \int_{-\infty}^{\infty} dh \nu W(h\nu_{\text{probe}}, t) \delta[\Delta \tilde{V}_{nm}(R) \\ &\quad - h\nu] \delta[R - R_i(t')] \\ &= \frac{1}{N} \sum_{i=1}^N \int_{-\infty}^{+\infty} dt' \int_{-\infty}^{\infty} dR W(R, t) \delta[R - R_i(t')] \\ &= \frac{1}{N} \sum_{i=1}^N \int_{-\infty}^{+\infty} dt' \int_{-\infty}^{\infty} dR e^{-(t-t')^2/2\delta^2} e^{-(R-R^*)^2/2\Delta^2} \\ &\quad \times \delta[R - R_i(t')] \end{aligned} \quad (4)$$

in which the one-dimensional resonance condition is used to transform the probe laser spectral distribution to coordinate space, where it is further approximated that the window function is a Gaussian in space and time, which is centered at  $R^*$  along the I-I coordinate with a spatial width of  $\Delta$ .<sup>22</sup> Note,  $\Delta \tilde{V}(R)$  is the difference between a pair of solvated iodine states. While educated guesses can be made about the solvated potentials, for configurations reached in ultrafast pump-probe studies there usually is no independent information. In practice, the inversion is made with an ensemble of trajectories for the I<sub>2</sub> internal coordinate, with  $\Delta$  and  $R^*$  as adjustable parameters. A faithful reproduction of the observed transients is then taken as a consistency check in the interpretation of the underlying dynamics and the effective solvated potentials.

All of the data to be reported here are single color pump-probe measurements, where at  $t=0$  each of the laser pulses serve as both pump and probe. Accordingly,  $S(t)$  is symmetric with respect to the time origin. This consideration is most conveniently accommodated by first reflecting the trajectory ensemble about  $t=0$ , and then carrying out the convolution of Eq. (4), using the experimentally measured auto correlation width of the laser for  $\delta$ .

The classical simulations are carried out on a single electronic surface, the  $B$  state potential of I<sub>2</sub>. Yet, we expect significant predissociation in the liquid phase. In the effective one dimensional treatment of transients, the Landau-Zener model for curve crossings is the natural framework to

use.<sup>23</sup> Accordingly, for population prepared and probed in the  $B$  state, the signal may be fitted by weighting the trajectories based on the number of crossings they undergo before reaching the probe window

$$S(t) = \frac{1}{N} \sum_{i=1}^N \int_{-\infty}^{+\infty} dt' \int_{-\infty}^{\infty} dR W(R,t) P_i(t') \delta[R - R_i(t')] \quad (5)$$

in which the weight of the  $i$ th trajectory at time  $t$  is given as the product over the  $j$  prior passages over the crossing point  $R = R_c$  with instantaneous velocity  $v_c$

$$P(t) = \prod_j P_{12}(v_c(j)), \quad (6)$$

where  $P_{12}$  is the Landau–Zener probability of remaining on the initial surface

$$P_{12}(v_c) = \exp\left(-\frac{4\pi^2 \langle V_{12} \rangle^2}{h|v_c(\partial V_2/\partial R - \partial V_1/\partial R)|_{R=R_c}}\right). \quad (7)$$

While consistent with the method used for the inversion of trajectories, this one dimensional curve crossing probability is only an approximation of the many-body problem at hand. Nevertheless, as in the case of the reduction of the many-body resonances using an effective solvated potential, we expect this treatment of predissociation to be useful in understanding the transients, with the caveat that the coupling matrix elements,  $\langle V_{12} \rangle$ , that are extracted must be regarded as *effective matrix elements between solvated potentials averaged over solute–solvent configurations*.

## IV. EXPERIMENTAL RESULTS

### A. Pump–probe transients in $CCl_4$

Two-photon excitation of  $I_2$  in room temperature liquid solutions leads to near infrared emission from the thermally equilibrated  $0_g^+$ ,  $0_u^-$ , and  $1_u$  surfaces that arise from the interaction of a pair of spin–orbit excited iodine atoms.<sup>16</sup> The liquid phase single color pump–probe studies which we report here, rely exclusively on this fluorescence as detection. In Fig. 3 we show pump–probe transients obtained at wavelengths ranging from 640 to 480 nm, i.e., for preparation of the molecule in its  $B$  state, from the potential minimum to above the dissociation limit. The transients decay within  $200 \text{ fs} < t < 700 \text{ fs}$ , after showing a few oscillations. In all cases there is a contribution to the signal at  $t=0$ , therefore a probe resonance near the inner branch of the  $B$  potential. As the wavelength is shortened, a dip develops at  $t=0$ , due to a delayed resonance which occurs at a time less than half the vibrational period. This would indicate that a second probe window opens for stretched geometries of the molecule. The relative contribution from the outer window decreases progressively as the excitation energy is lowered, such that at 580 nm, only the inner window contributes to the signal. Also noticeable is the distinctly different appearance of the transients at wavelengths ranging from 600 to 640 nm. Here, after the  $t=0$  signal, the packet returns to the inner

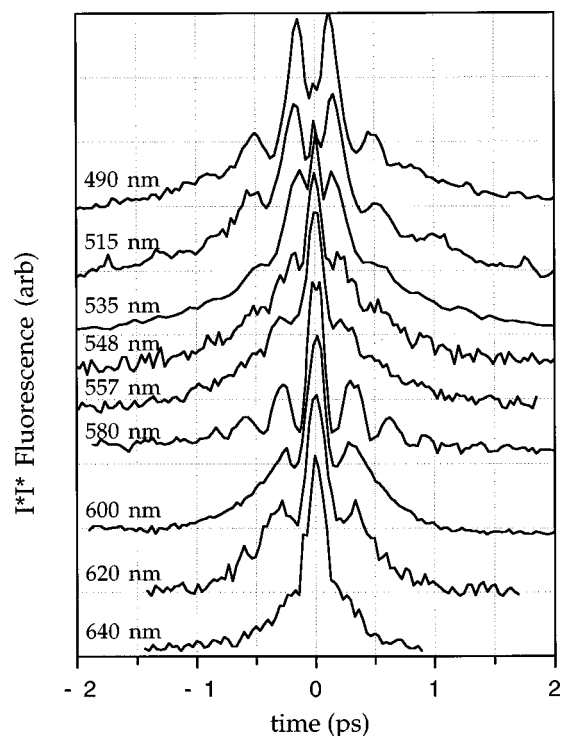


FIG. 3. Single color pump–probe transients in liquid  $CCl_4$ .

turning point in a vibrational period, yet it no longer shows any oscillations. We will fix the locations of the windows with the aid of simulations, then rationalize the implied resonances. What is clear at the onset is that since the  $B$  state is initially prepared, the rapid decay of the signal results from population loss, the result of predissociation. Reliable decay times can be extracted from the data, as we describe below. Inspection is, however, sufficient to conclude that the higher the initial preparation energy in the  $B$  state, the longer is the electronic lifetime: the observed predissociation is dominated by a crossing near the potential minimum.

### B. Pump–probe transient in solid Kr

The rapid predissociation observed in liquid  $CCl_4$  is to be contrasted with what is observed in solid Kr. Since the previously reported data in Kr were obtained by two-color measurements,<sup>6</sup> to ensure that the comparison is direct, here we provide a single color measurement. In Fig. 4 we show a transient from solid Kr, using 556 nm to pump and to probe, with the  $E(0_g)$  ion-pair state acting as the upper state in the probe transition. This transient is nearly identical to what was previously reported in the two-color experiments,<sup>6</sup> and yields itself to the same interpretation presented there. Additionally, the one-color experiment clearly marks the origin of time, and uniquely identifies the probe window location on the outer turning point of the  $B$  potential. It is unambiguous that the observed transient is in the initially accessed state, the  $B$  state, and not the result of trapping in the lower electronic manifold after predissociation, as assumed by Batista and Coker in their interpretation of our published data.<sup>9(b)</sup>

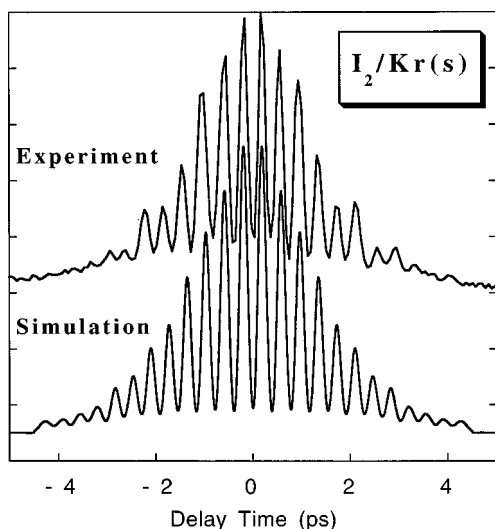


FIG. 4. Single color pump-probe transients in solid Kr, obtained at 556 nm, and using ion-pair state fluorescence for detection.

## V. ANALYSIS

Gross features of the liquid phase  $B$  state dynamics can be directly read from the experimental transients in Fig. 3. The data indicate that: (a) predissociation of the  $B$  state occurs on a time scale of  $\sim 0.5$  ps; (b) when prepared near the middle of the potential, at 580 nm, predissociation proceeds with complete retention of vibrational coherence; (c) when prepared in the anharmonic part of the  $B$  state, near its dissociation limit or above, nuclear coherence is lost on the time scale of predissociation; (d) predissociation is most rapid at the bottom of the potential. Furthermore, by comparison with the data in Fig. 4, it is possible to conclude that predissociation in solid Kr is an order of magnitude slower than in liquid  $CCl_4$ . To further characterize the system parameters, it is necessary to quantify energy dissipation from  $I_2$  to the solvent, and to locate the curves responsible for predissociation. This information is more subtly encoded in the experiments, and requires scrutiny through simulations. We begin with a discussion of the anticipated resonances, prior to dissection of the pump-probe transients.

### A. Excitation resonances

If we restrict ourselves to  $\Delta\Omega=0$  transitions and  $u \leftrightarrow g$  selection rules, in the spectral range of the experiments, three transitions probe the  $B$  state:  $a'(0_g^+) \leftarrow B(0_u^+)$ ,  $I^*I^*(0_g^+) \leftarrow B(0_u^+)$  and  $E(0_g^+) \leftarrow B(0_u^+)$ . The latter only becomes accessible due to solvation of the ion-pair states in the dielectric of the medium, the extent of which may be estimated from the Onsager cavity model<sup>24</sup>

$$E_s = -\frac{8\mu^2}{d^3} \frac{(\epsilon-1)}{(2\epsilon+1)} \approx \frac{e^2}{r_e} \frac{(n^2-1)}{(2n^2+1)} \quad (8)$$

in which the cavity diameter is approximated as  $d=2r_e$ , where  $r_e=3.6$  Å, is the equilibrium bondlength of the ion-pair state.<sup>25</sup> Using the index of refraction of  $CCl_4$ ,  $n=1.46$ , a vertical electronic solvation of  $\sim 7000$   $cm^{-1}$  can be anticipated. This estimate is quite sensitive to the choice of cavity

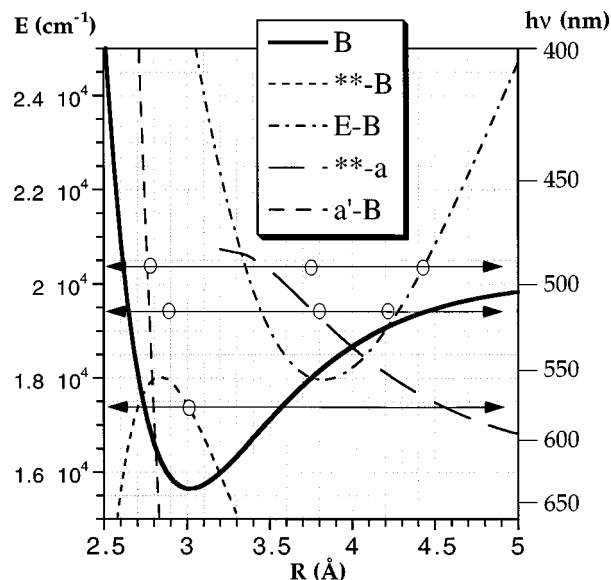


FIG. 5. Difference potentials that serve as probe transitions. In the legend, \*\* refers to  $I^*I^*$ . The probe window locations extracted from the simulations of the data are shown as open circles.

radius, which is an ill-defined quantity. A vertical shift of  $\sim 6000$   $cm^{-1}$  is more consistent with the resonances extracted from the dynamical simulations, as will be elaborated below, and well within the uncertainty in the cavity model. We have used this shift in Fig. 5 to show the predicted  $E-B$  difference potential, which is double valued for all probe wavelengths.

The only resonance that is accessible after predissociation, from states that correlate with  $I(^2P_{1/2})+I(^2P_{1/2})$ , is the  $I^*I^*(1_u) \leftarrow I_2(a(1_g))$  transition. This difference potential, valid after the crossing point,  $R_c=3.16$  Å,<sup>26</sup> is single valued as shown in Fig. 5. Since at large internuclear distances this transition corresponds to a double spin-flip, it can be expected to be rather weak. While selection rules allow the connection of all states correlating with the ground state atoms to ion-pair states, none of these resonances lie in the wavelength range of our studies.

The presence of a peak at the time origin of all transients shown in Fig. 3, suggests the presence of a probe window on the repulsive wall of the  $B$  state throughout the wavelength range 640–490 nm. The  $a' \leftarrow B$  transition can act as such a resonance, as illustrated in Fig. 5. The requirement for this fluorescence channel is that the excitation terminate above the crossing between  $a'$  and  $I^*I^*$  surfaces (see Fig. 1). Also, at the short internuclear distances corresponding to inner turning points of the  $B$  state,  $\Lambda-\Sigma$  coupling will prevail, and strict Hund's case (c) considerations are no longer valid. Under case (a) we can find a variety of transitions that couple the repulsive wall of the  $B$  state to the repulsive potentials that arise from both  $I+I$  and  $I^*+I$  limits, above their crossing with the  $I^*+I^*$  potentials. The inner resonances leading to a signal at time origin can be rationalized, however, the curves at these short internuclear distances are poorly known, and the difference potentials in Fig. 5 are only used as guidance. Quite clearly, multiple probe windows will be

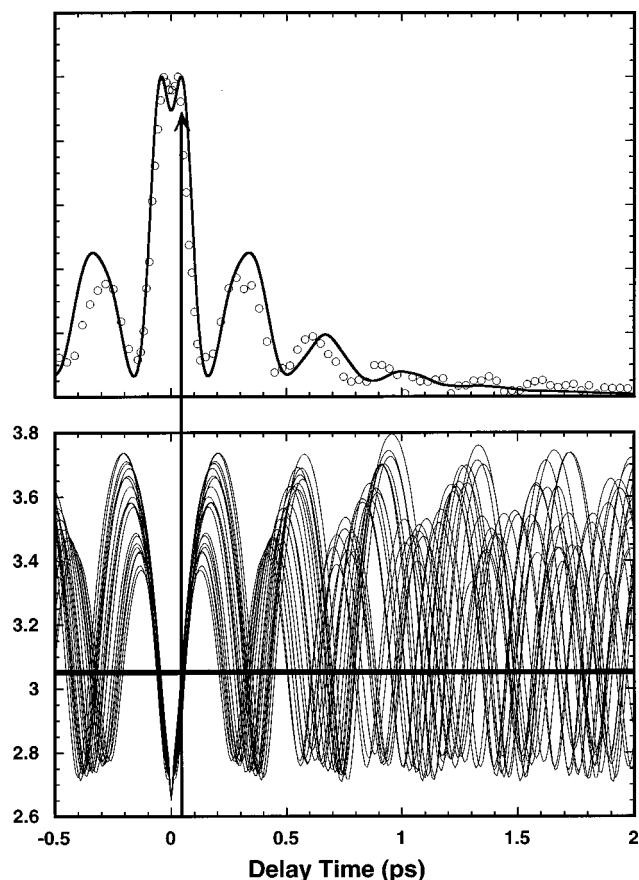


FIG. 6. Analysis of the 580 nm transient using molecular dynamics simulation. The experimental data points are shown as open circles in the top panel. The simulated signal is shown as the continuous line (based on 360 trajectories). In the lower panel, a set of representative trajectories, folded at  $t=0$ , is shown. The dip at  $t=0$  in the data helps to fix the probe window location with accuracy. A delay in the appearance of the resonance of  $\sim 50$  fs (vertical line), locates the probe window at  $3.05$  Å (horizontal line in lower panel).

active in the detected signals, and should be taken into consideration in the interpretation of data.

### B. The 580 nm transient, coherent predissociation and vibrational relaxation

The 580 nm transient shows the most regular oscillations, with evidence of only one active probe window. An expansion of the transient, shown in Fig. 6, resolves a dip in the signal at  $t=0$ . This would signify a time delay between launching the wave packet on the  $B$  surface and its arrival to the probe window. With the help of trajectories shown in Fig. 6(b), this delay allows an accurate location of the probe window at  $R^*=3.05$  Å, (see vertical arrow in Fig. 6). Since the temporal width of the probe window is fixed by the measured auto correlation of the laser pulse as 95 fs, only two variables remain to simulate the signal: the spatial width of the probe window,  $\Delta$ , and the predissociation probability. An adequate reproduction is obtained, as shown in Fig. 6(a), when using  $\Delta=0.075$  Å, and assuming predissociation via

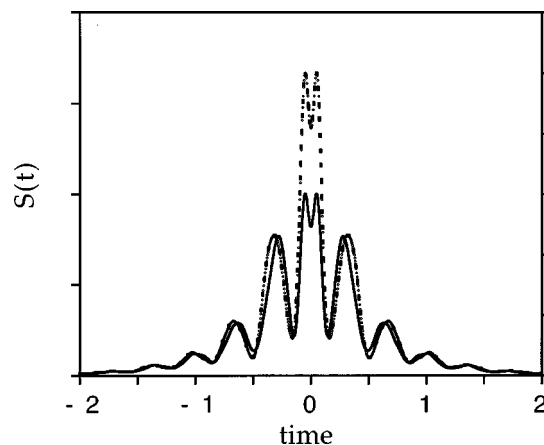


FIG. 7. Expected signals for curve crossing before arriving to the probe window (solid line) and after passing through the probe window (dashed line).

$a(1_g)$  with an effective coupling matrix element  $|\langle V_{B-a} \rangle| = 175 \text{ cm}^{-1}$  ( $R_c = 3.16$  Å, and  $\Delta|dV/dR| = 13\,200 \text{ cm}^{-1} \text{ Å}^{-1}$ ).

While the predissociation probability per crossing is well determined by the above analysis, the assumed parameters of the one dimensional Landau–Zener model are not independently determined. However, with respect to the location of the crossing,  $R_c$ , the analysis firmly establishes that it must occur at an internuclear distance greater than the probe window, i.e.,  $R_c > R^* = 3.05$  Å. Had this not been the case, a very different intensity ratio would have been observed for the first two resonances, as illustrated in Fig. 7. The difference between these two conditions arises from the fact that the first resonance is due to the outgoing packet alone, while the subsequent resonances consist of both outgoing and inward moving packets [see Fig. 6(b)]. The first resonance corresponds to a half-period sampling of the potential, while the second is a full-period sampling. Thus the relative ratio of the first resonance to latter resonances will depend on whether  $R_c$  occurs before or after the first observation of the packet at  $R^*$ . Only the latter case is consistent with the data.

We may safely conclude that: (a) the predissociation occurs at  $R_c > 3.05$  Å, and therefore cannot be due to the  $B''(1_u)$  surface [see Fig. 1]; (b) the parameters used yield the correct magnitude of predissociation,  $\sim 60\%$  per period.

Vibrational energy relaxation is an integral part of the observed signals and their interpretation. Since  $CCl_4$  is treated as structureless, it may be expected that the vibrational energy transfer to the solvent is underestimated. This could affect the interpretation of predissociation parameters extracted from fits, since the LZ probabilities are determined by instantaneous velocities at  $R_c$ , which in turn are determined by the instantaneous vibrational energy content in the molecule. The time dependence of the period between oscillations of the signal contains this information, and can, in this case, be extracted from an analytical fit to the experiment. Taking into account the inverse velocity dependence of the signal intensity,<sup>22</sup> and an exponential decay of popu-

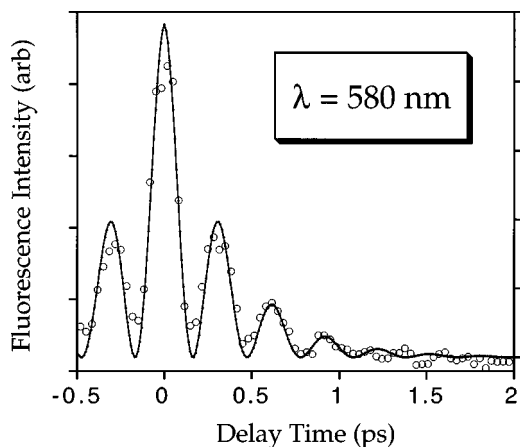


FIG. 8. Fit of the 580 nm transient to the analytic form of Eq. (9) in the text.

lation due to predissociation, the oscillatory signal can be represented as

$$S(t) = \frac{e^{-t/\tau_{LZ}}}{\sqrt{E(t) - V^*}} [1 + f(t)\sin(\omega(t)t + \varphi)] \quad (9)$$

in which  $V^*$  is the value of the potential at the probe window location,  $R^*$ ;  $f(t)$  describes the decay of the modulation depth due to decay of coherence among the trajectories in phase space; and  $E(t)$  describes the dissipation of vibrational energy. For a given function of  $E(t)$ , the time dependent angular frequency is obtained for the Morse oscillator as

$$\begin{aligned} \frac{\omega(t)}{2\pi c} &= \omega_e - 2\omega_e x_e n(t) \\ &= \omega_e x_e \\ &\quad + \sqrt{(\omega_e - \omega_e x_e)^2 - 4\omega_e x_e [E(t) - \omega_e/2 - \omega_e x_e/4]}. \end{aligned} \quad (10)$$

The 580 nm data can be well fit by this expression under the assumptions of complete coherence and exponential energy decay

$$f(t) = 1, \quad \text{and} \quad E(t) = E_0 \exp(-t/\tau_v). \quad (11)$$

With a vibrational energy relaxation time of  $\tau_v = 10$  ps, a predissociation time constant  $\tau_{LZ} = 320$  fs (and  $\varphi = 1.4$  rad), the experimental data can be well described (see Fig. 8). The functional fit enables the simultaneous extraction of energy dissipation and predissociation rates, without resorting to simulations. The extracted value of  $\tau_{LZ} = 320$  fs corresponds to the vibrational period of  $\tau_n = 313$  fs of the initially prepared vibration ( $n = 13$  prepared at 580 nm), therefore consistent with the predissociation probability of  $\sim 60\%$  per period derived above. The data is not sensitive to the energy dissipation rate as long as  $\tau_v/\tau_{LZ} > 10$ ; i.e., energy relaxation is insignificant within the electronic predissociation time. An equally good fit to the data is obtained when using for  $E(t)$  a functional fit to the energy loss curve obtained from the MD simulations, which is better described as a double exponential decay (see below). In short, the vibrational energy in the

$B$  state, and therefore the instantaneous velocities at  $R_c$ , are reliably treated in the simulations. The experiment does not determine  $\tau_v$  with any accuracy since the observation time is limited by predissociation, which is much faster than vibrational relaxation.

Finally, the analysis fixes the probe window at  $R^* = 3.05$  Å for a probe wavelength of 580 nm ( $17250 \pm 250$   $\text{cm}^{-1}$ ). To rationalize this window location it was necessary to assume a somewhat steeper curve for the repulsive  $I^*I^*(0_g^+)$  potential in Fig. 5 than Mulliken's original guess.<sup>15</sup>

### C. The 556 nm transient, coherent dynamics in solid Kr

The solid state data is included here to make direct comparisons. We simulate the signal in this case using the well determined parameters of the probe window,  $R^* = 3.7$  Å and the same curve crossing parameters as in the liquid case, except for the effective coupling element,  $|\langle V_{12} \rangle|$ . Now, the experimental transient is reproduced as shown in Fig. 4 when  $|\langle V_{12} \rangle| = 65$   $\text{cm}^{-1}$  is used. The parameters used in the present are similar to those previously extracted in the analysis of predissociation in Kr, where the measurements were conducted using a uv probe laser tuned to the  $f(0_g)$  ion-pair state.<sup>6</sup> In the present single color measurement the probe accesses the minimum of  $E(0_g)$  ion-pair state. In our prior treatment we assumed exponential decay of the  $B$  state population due to predissociation, and extracted a value of  $|\langle V_{12} \rangle| = 54 \pm 7$   $\text{cm}^{-1}$ . Here, we explicitly treat the curve crossing during the simulations.

### D. The 515 and 490 nm transients, loss of coherence

Similar transients are observed at 490 and 515 nm, for initial preparations above the  $B$  state dissociation limit and near it, respectively. In both cases a sharp peak at  $t = 0$  is observed, followed by a broader peak at  $t = 130$ – $160$  fs, i.e., at a time delay shorter than half the vibrational period. This would imply the presence of at least two probe windows, one on the repulsive wall and one on the attractive wall of the  $B$  potential. Based on the difference potentials shown in Fig. 5, if we ascribe the outer resonance to the  $E \leftarrow B$  transition, then this window further splits into two, necessitating a minimum of three probe windows in the simulation. The data also show a resonance after a time delay of 0.5 ps, which can be ascribed to a recursion to the outer window after a full period in the bound region of the potential. This peak arises from the fraction of the molecules that undergo head-on collision. No further oscillations are evident, and the signal decays exponentially past  $t = 0.5$  ps. The signals are simulated by including weighted contributions from three probe windows, while using the same predissociation parameters as in the 580 nm data (see Fig. 9). The results are not sensitive to the parameters of the inner window, which is fixed at  $R^* = 2.75$  and  $2.9$  Å, for the 490 and 515 nm data, respectively. The outer probe window parameters are adjusted. The assumed locations of the probe windows are marked in Fig. 5. They are only approximately predicted by the vertically sol-

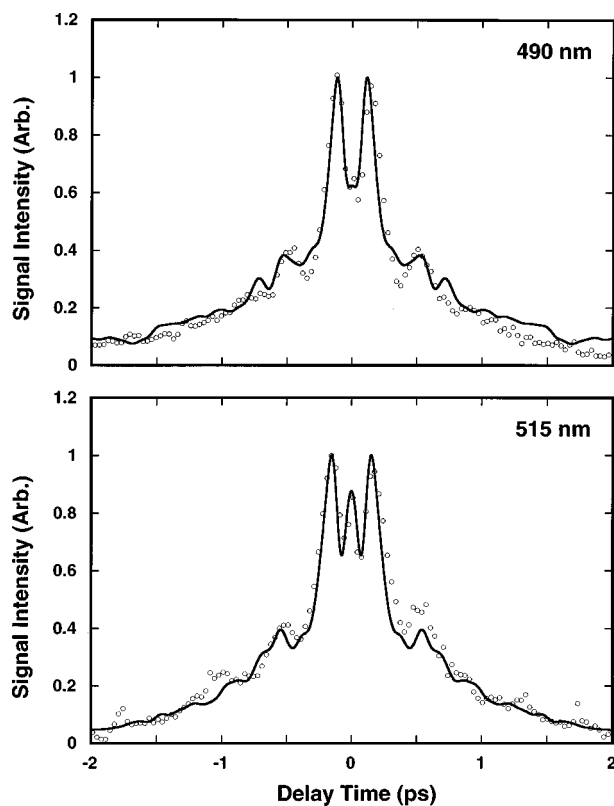


FIG. 9. Simulation of the 490 and 515 nm transients, using the three indicated windows in Fig. 5.

vated one-dimensional difference potential. As in the case of solid state analysis, the data suggests that solvation is accompanied by a stretch of  $0.1\text{--}0.2 \text{ \AA}$  in the ion-pair bond length.<sup>27</sup>

According to Fig. 5, at these probe wavelengths, wavepackets on the  $a(1g)$  surface could also contribute to the signal; however, a careful analysis shows that this contribution will be masked by the  $E \leftarrow B$  resonance (see the Appendix). The transient has little information content about the final electronic state.

The adequate reproduction of the observed transients in Fig. 9 establishes that the predissociation parameters used in the analysis of the 580 nm transient are also consistent with those at 515 and 490 nm.

A major difference between dynamics when the system is prepared in the deeply bound part of the  $B$  potential, at 580 nm, versus those created in the anharmonic part near dissociation is that the vibrational coherence decays prior to predissociation. In fact, the classical vibrational coherence, a measure of which is the time dependent ensemble average of the molecular bond length  $\langle R(t) \rangle$ , is lost after the first period of motion in the simulations. Given the similarity in masses of I atoms and  $CCl_4$ , extensive energy loss occurs in the first collision with the solvent, and the thermal distribution of impact parameters is sufficient to ensure that the dispersion in recombination times (or recursion times to the inner turning point) is larger than the subsequent vibrational half-period. As a result  $\langle R(t) \rangle$  does not show any oscillations. This is in contrast with the solid state, in which it has been

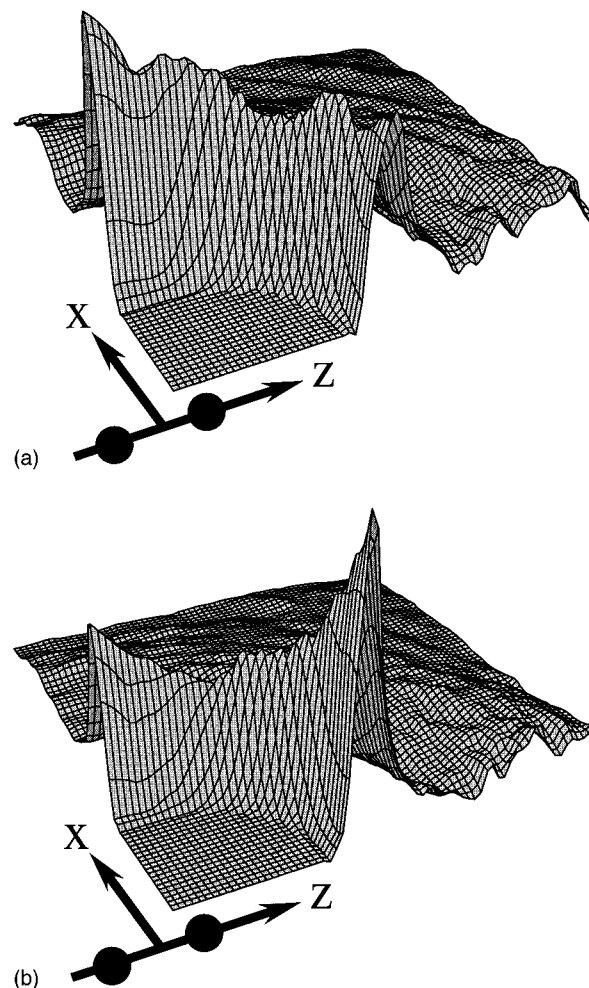


FIG. 10. Structure of the  $CCl_4$  solvent for isotropic (top) and anisotropic (bottom)  $I_2(X)\text{--}CCl_4$  potentials obtained by Monte Carlo sampling ( $10^6$  configurations in each case). The same contour levels are used in both panels. The anisotropic potential leads to a maximum along the internuclear ( $z$ ) axis of the molecule and a reduction of density in the “T” geometry over the isotropic distribution.

shown that structural order of the solvent ensures sudden cage induced recombination, and therefore proceeds with preservation of vibrational coherence.<sup>27</sup> A sudden recombination wave, arising from the fraction of molecules that suffer head-on collisions, is present in the liquid phase and gives rise to the peak near  $t \sim 0.5$  ps. The contrast between this peak and the underlying tail is dictated by the structure of the first solvation shell, which in turn is dictated by the solute–solvent interaction potential in the ground electronic state. To reproduce the signal, it was necessary to use the anisotropic  $I_2(X)\text{--}CCl_4$  potential which sustains minima of  $1.5 K_B T$  along the linear geometry (see  $V_\Sigma$  in Table I). A comparison of the thermal solvent structure forced by the anisotropic and isotropic potentials is shown in Fig. 10. The anisotropic  $I_2\text{--}CCl_4$  potential produces significant structuring of the first solvation shell, leading to maxima in the angular distribution along the molecular axis. To optimize avoided volume, a  $\sim 30\%$  reduction of the distribution in the “T”-geometry relative to that of the isotropic potential occurs.

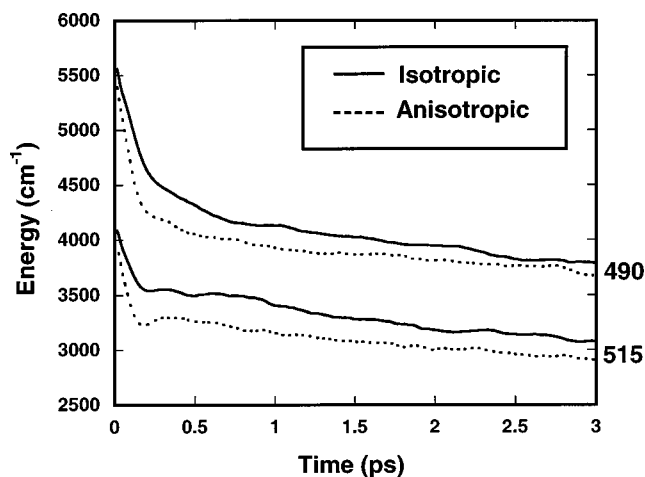


FIG. 11. Vibrational energy decay for initial preparations at 490 and 515 nm, above and below the dissociation limit of the molecule. The initial energy drop occurs upon collision with the solvent, in  $\sim 100$  fs, the subsequent relaxation in the expanded cage is slow on the predissociation time scale. The extent of initial energy loss depends on the extent of anharmonicity at the preparation energy, and on the solvent structure: greater when using the anisotropic potential which leads to earlier head-on collisions.

The choice of the ground state solute-solvent potential also has a significant effect on energy dissipation in the excited state. This mechanical effect has recently been discussed in relation to the gas phase  $I_2$ -Ar complex, in an attempt to resolve the one-atom cage effect controversy.<sup>28</sup> In Fig. 11, we show plots of the time dependence of the ensemble averaged  $I_2$  energy,  $\langle E(t) \rangle$ , for the 490 and 515 nm simulations, and with isotropic and anisotropic  $I_2$ - $CCl_4$  potentials in the ground state. The curves are typical for dissipation of Morse oscillators in condensed phase.<sup>29</sup> Here, the dynamics is quite clear. Extensive energy loss occurs during the first collision, which terminates with the molecule reaching a relatively harmonic part of its potential, in a relaxed solvent cage. Subsequent energy loss occurs at a much slower rate. The extent of energy loss in the first collision depends on impact parameters and the timing of the collision. For a head-on collision, the earlier the collision during the extension of the I-I bond, the larger is the available kinetic energy to transfer to the solvent. Thus, as illustrated in Fig. 11, the anisotropic potential which gives a tighter collinear alignment, leads to more efficient energy loss. In analyzing the energy dependence of predissociation probabilities, it is the internal energy during curve crossings that is required, rather than the energy of preparation. Thus while the 490 nm excitation prepares the molecule with an internal energy content of  $5000 \text{ cm}^{-1}$ , the predissociation rate of 680 fs which can be extracted from an exponential fit to the data, occurs at the characteristic energy of  $\tilde{E} \sim 4000 \text{ cm}^{-1}$  (see Fig. 11). We will use this consideration in the analysis of energy dependence of predissociation probabilities.

### E. The 640–600 nm transients

Excitation at 640 nm corresponds to preparation of the molecule near  $v=0$ . It is clear from the transient in Fig. 3,

that with this preparation, the molecule predissociates with nearly unit probability. Since no recursions can be seen, the predissociation probability must be  $\sim 100\%$  per period.

Excitation at 600 nm prepares the molecule near  $v=10$ . In this case a first recursion of the wave packet is clearly observed. This signal, which appears after a time delay of a vibrational period, is much broader than the resonances observed at shorter wavelengths. If we were to ignore nonadiabatic dynamics, we would be led to the conclusion that the 600 nm preparation leads to a faster loss of coherence than the 580 nm preparation, despite the fact that it is created in the more harmonic part of the potential. The more likely interpretation is that we are seeing trapping of population in the adiabats created at the intersection of the two potentials. A similar situation has recently been studied in time resolved experiments on IBr in the gas phase.<sup>30</sup> In contrast with the gas phase, in condensed media, sharp interferences are not expected since the crossing is strongly modulated by the solvent. The classical simulations used in the present work are ill suited for a realistic analysis of these effects.

### F. Energy dependence of predissociation

The expression of Eq. (9) is sufficiently flexible to enable a phenomenological fit of the experimental transients. We carry out such an analysis mainly to establish the energy dependence of predissociation rates. We treat the vibrational relaxation as a double exponential, an initial decay with a time constant of 100 fs, followed by a slow decay with  $\tau > 10$  ps. To fit the data faithfully, it is necessary to include an exponential damping of the modulation, using  $f(t) = \exp(-t/T_2)$  in Eq. (9). Operationally,  $T_2$  establishes damping of modulation, it incorporates effects of temporal and spatial resolution, and decay of vibrational coherence. It should not be interpreted as a true measure of coherence decay. The data can be well fit by this method, as illustrated by examples in Fig. 12. Table II contains the extracted parameters. The extracted time constants of predissociation are comparable to vibrational periods (see Table II), as such they have little meaning as rate processes. The more meaningful number is the predissociation probability per crossing, namely,

$$P_{12} = \frac{1}{2\omega(\tilde{E})\tau_{LZ}} \quad (12)$$

in which the frequencies are calculated from the characteristic energies using the  $I_2(B)$  Morse parameters. The extracted probabilities are plotted as a function of characteristic energy,  $\tilde{E}$ , in Fig. 13. Since the probabilities monotonically increase as  $v=0$  is approached, the data is consistent with a crossing near  $v=0$ . However, the variation of  $P_{12}$  with energy is too small. In the standard LZ model, for a fixed coupling constant, a hyperbolic dependence on velocity, therefore on  $\sqrt{\tilde{E}}$  is to be expected. Since the kinetic energy is varied in the experiment from  $\sim 150$  to  $4000 \text{ cm}^{-1}$ , at least a fivefold variation in probabilities is to be expected yet the observed variation in  $P_{12}$  ranges only from 0.65 to 0.4. The

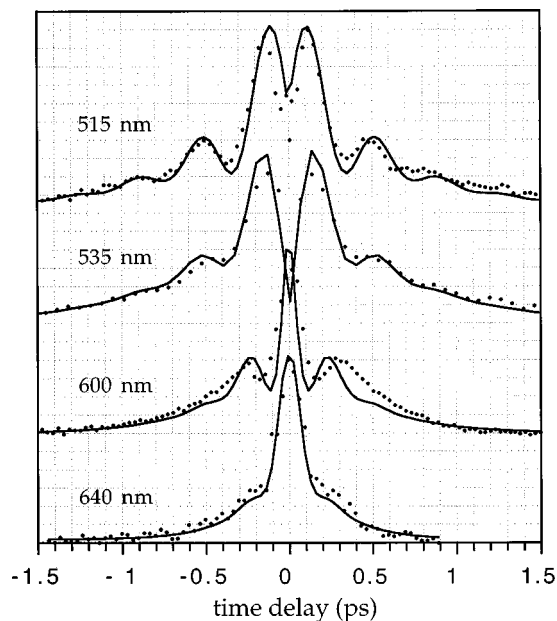


FIG. 12. Examples of fits to the data using Eq. (9), from which the energy dependent predissociation probabilities are extracted.

data simply cannot be fit under the assumption of a fixed coupling constant. Anticipating the discussion in the next section, it is possible to fit the data under the assumption that the effective coupling is determined by driven solvent dynamics, and that the dynamical coupling scales with the vibrational amplitude of  $I_2$ , i.e., as  $E^{1/2}$ . Thus we assume a modified LZ model, in which the dynamical coupling,  $\langle V_{12} \rangle^d$ , is a linear function of vibrational amplitude where,

$$\langle V_{12} \rangle^d = \langle V_{12} \rangle^e (1 + a\sqrt{E}) \quad (13)$$

in which  $\langle V_{12} \rangle^e$  is the effective coupling constant given by the structure of the solvent at equilibrium with the ground state  $I_2$ . The data fits this model, as illustrated in Fig. 13, with  $\langle V_{12} \rangle^e = 175 \text{ cm}^{-1}$ ,  $a = 0.0082 \text{ cm}^{-1/2}$  (based on  $|\Delta(\partial V/\partial r)| = 13\,200 \text{ cm}^{-1} \text{ \AA}^{-1}$ ). The required increase of

TABLE II. Parameters extracted from analytical fit to transients [Eq. (9) of the text].

$\lambda(\text{nm})^a$	$\langle E \rangle(\text{cm}^{-1})^b$	$1/c\omega(\text{fs})^c$	$\tau_{LZ}(\text{fs})^d$	$P_{LZ}^e$	$T_2(\text{fs})^f$
490	4000	620	680	0.44	500
515	3300	460	580	0.39	500
535	2800	400	510	0.39	500
548	2600	381	480	0.39	400
557	2350	362	400	0.45	400
580	1640	320	330	0.48	-
600	1166	299	310	0.48	220
620	700	281	280	0.50	170
640	150	265	210	0.63	100

<sup>a</sup>Excitation wavelength.

<sup>b</sup>Characteristic energy after energy loss in first collision, and assuming  $T_e(B) = 15\,400 \text{ cm}^{-1}$ .

<sup>c</sup>Vibrational half-period at characteristic energy.

<sup>d</sup>Predissociation time constant obtained from the fit to Eq. (9) of the text.

<sup>e</sup>Experimental predissociation probability per crossing.

<sup>f</sup>Damping constant of observed modulation.

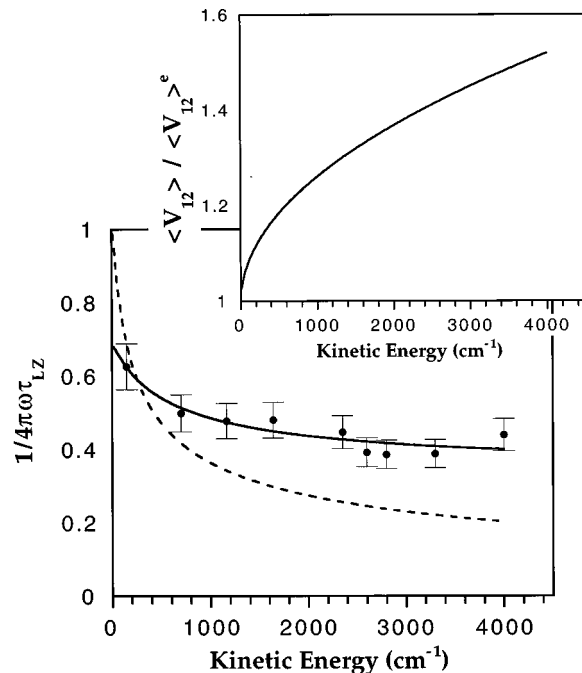


FIG. 13. The energy dependence of predissociation probabilities per crossing does not fit the standard Landau-Zener expectation (dashed line). The data can be fit using a dynamical coupling which is a linear function of  $E^{1/2}$  (vibrational amplitude), and is shown in the inset (normalized to the coupling constant at equilibrium).

the effective coupling constant (see inset to Fig. 13) is  $\sim 50\%$ , between preparations of the molecule at the bottom and near the top of the potential.

## V. DISCUSSION

Analysis of the  $B$  state transients is possible under the assumption of a single predissociation channel, located near  $v=0$ . This does not preclude the presence of weaker channels, due to other crossings. In fact, in solid state measurements where the vibrational dynamics proceeds with tighter coherence, several weaker crossings are clearly observed.<sup>31</sup> In the liquid phase, the likely candidates for the main predissociation channel can be narrowed to  $B''(1_u)$ ,  $2_g$  and  $a(1_g)$  surfaces (see Fig. 1). Of these, the  $B''$  surface may be eliminated based on the analysis of the 580 nm transient, which established the crossing to be at  $R > 3.05 \text{ \AA}$ . The  $B''$  crossing had previously been invoked as being active in this system to rationalize the observed nonmonotonic decay of intensities in resonant Raman progressions of  $I_2$  in  $CCl_4$ .<sup>32</sup> A recent theoretical analysis allows the reinterpretation of that data as interference in scattering from the two  $RR$  active surfaces,  $B''$  and  $B$ , without invoking coupling between them.<sup>33</sup> The extant data and analysis does not allow a direct distinction between  $a(1_g)$  and  $2_g$  channels of predissociation. The first of these is commonly preferred, since it would involve the change of only one unit of angular momentum. However, DIM analysis shows that the  $2_g$  surface can also be active.<sup>10</sup> In either case, the crossing involves a solvent induced  $u \rightarrow g$  and  $\Delta\Omega \neq 0$  transition. Accordingly, the off-diagonal potential surface that induces the predissociation must fulfill two

criteria: It must have  $u$  symmetry and must act along the perpendicular to the molecular axis. Note, these requirements are contingent upon the preservation of the molecular inversion symmetry and  $\Omega$  as a good quantum number, conditions which are well established by the spectroscopy of  $I_2$  in these weakly interacting solvents. The two identified criteria are key to rationalizing the difference between observed probabilities of predissociation in liquid  $CCl_4$  versus solid Kr, as we expand below.

The result that predissociation in liquid  $CCl_4$  is faster than in solid Kr is unexpected if many-body probabilities are assumed to result from the scalar sum of probabilities over perturbers. To see this, consider a coupling matrix element which is only a function of separation between  $I_2$  and quencher. For a polarizable quencher, which does not itself undergo electronic transitions, the expectation is that  $V \propto \alpha_Q/R^6$ .<sup>34</sup> The effective coupling in the two phases, prior to disturbance of the solvent by the  $I_2$  dynamics, can be related as

$$\frac{\langle V \rangle_l}{\langle V \rangle_s} \approx \frac{\alpha_l \langle \sum_i R_i^{-6} \delta[R - R_i] \rangle_l}{\alpha_s \langle \sum_i R_i^{-6} \delta[R - R_i] \rangle_s} \quad (14)$$

in which the summation inside the angle brackets is over all positions of the solvent for an instantaneous configuration, and the angular brackets imply ensemble averaging by taking the average over realized configurations; ( $l$ ) represents liquid  $CCl_4$  and ( $s$ ) represents solid Kr. The strong  $R$  dependence implies that the coupling is determined by the local density of the solvent, mainly by the radial distribution of the first solvent shell, which in turn depends on the assumed intermolecular potentials. Despite the fact that the polarizability of  $CCl_4$ ,  $\alpha = 10.5 \text{ \AA}^3$ , is significantly larger than that of Kr,  $\alpha = 2.48 \text{ \AA}^3$ , the local density of the solvent dictates the ratio of Eq. (14) to be 0.23; i.e., the predissociation probability in the liquid phase would be expected to be a factor of  $\sim 20$  smaller (probability  $\propto \langle V \rangle^2$ ). Contrast this with the experimental observation that the predissociation probability in the liquid phase is a factor of 10 larger.

Similar conclusions are reached if the off-diagonal surface is taken to have  $g$  symmetry, as in the real positive function assumed in the treatment by Ben-Nun and Levine (BL).<sup>11</sup> While they assume the predissociation to proceed via  $B(0_u) \rightarrow a(1_g)$ , they use the expression given by Yardley for the leading term in the perturbative analysis of electronic quenching by a polarizable collision partner<sup>34,35</sup>

$$V_{B-a} = -\frac{3}{2} \frac{I_B I_Q}{(I_B + I_Q)} \frac{\alpha_{B-a} \alpha_Q}{R_{I_2-Q}^6} \quad (15a)$$

with the further decomposition

$$\alpha_{B-a} = \alpha_{\parallel} \cos^2(\vartheta) + \alpha_{\perp} \sin^2(\vartheta) \quad (15b)$$

in which the polarizability of the quencher,  $\alpha_Q$ , is coupled to the polarizability associated with the real transition between electronic states  $B$  and  $a$  of  $I_2$ , and  $I_Q$  and  $I_B$  represent the ionization potentials of the solvent and  $I_2(B)$ , respectively.<sup>35</sup> Using the value they recommend for the anisotropy of the transition polarizability ( $\alpha_{\parallel}/\alpha_{\perp} = 1.8$ ). After explicitly

evaluating the ensemble averages over liquid and solid state distributions, but now taking the angular anisotropy into account

$$\frac{\langle V \rangle_l}{\langle V \rangle_s} \approx \frac{\alpha_l \langle \sum_i \alpha_{B-a}(\vartheta) R_i^{-6} \delta[\mathbf{R} - \mathbf{R}_i] \rangle_l}{\alpha_s \langle \sum_i \alpha_{B-a}(\vartheta) R_i^{-6} \delta[\mathbf{R} - \mathbf{R}_i] \rangle_s} \quad (16)$$

we obtain that the predissociation probability in the solid state should be a factor of  $\sim 7$  larger than in the liquid. Thus as in the case of strictly additive probabilities, the discrepancy with experiment is nearly 2 orders of magnitude and in the wrong direction. Indeed, the ratio predicted in Eq. (16) is smaller than that of Eq. (14). This is a result of the assumption that  $\alpha_{\parallel} > \alpha_{\perp}$  and that the solute-solvent potential we use leads to a local solvent distribution peaked along the molecular axis in the liquid phase (see Fig. 10). Note, however, this effect is somewhat artificial, since as we argued above, for a  $\Delta\Omega = 1$  transition the parallel component of the transition dipole, and hence  $\alpha_{\parallel}$  must vanish.

The electrostatic model offered by Roncero, Halberstadt, and Beswick (RHB), in their treatment of the predissociation of the  $I_2$ -Ar complex, has the proper form for the electronic coupling.<sup>12</sup> In second-order perturbation, which is necessary to obtain a coupling through the solvent polarizability,<sup>34,35</sup> the leading electrostatic term for the requisite  $u \rightarrow g$  transition in  $I_2$  is the dipole-quadrupole operator; terms of the kind<sup>36</sup>

$$\langle Q\mu \rangle_{12} = \sum_i \frac{\langle B(0_u^+) | \hat{Q} | i_u \rangle \langle i_u | \hat{\mu} | a(1_g) \rangle}{(E - E_i)}. \quad (17)$$

RHB show that this leads to an  $R^{-7}$  distance dependence, and derive the angular dependence of the coupling surface under this electrostatic expansion<sup>12</sup>

$$V_{B-a}(\text{RHB}) = \frac{A \sin(\theta) [4 \cos^2(\theta) - 1]}{R^7}. \quad (18)$$

As desired, the angular dependence of the function is odd with respect to inversion (see Fig. 14). It is this signed, angularly anisotropic function that needs to be summed over the solvent distribution to obtain the effective coupling,  $\langle V_{12} \rangle$ , prior to squaring, to obtain transition probabilities. While a strictly electrostatic model, and therefore its validity may be debated, the form will lead to extensive cancellation when summed over a solvent distribution of high symmetry.

The off-diagonal DIM surface of Batista and Coker (BC) has the same symmetry properties.<sup>9(a)</sup> The angular dependence of their surface fits the form

$$V_{B-a}(\text{BC}) = \frac{A \sin(\theta) \cos^8(\theta)}{R^6} \quad (19)$$

and is shown in Fig. 14. In contrast with the RHB surface, it is sharply peaked at  $15^\circ$  and vanishes at  $90^\circ$ , it has an  $R^{-6}$  dependence, and a magnitude 2 orders larger at  $R = 5 \text{ \AA}$  (see comparison in Fig. 14). Given the very different origins of the functions, it is not too surprising that the BC and RHB forms differ in their detail, yet, both functions have the proper symmetry.

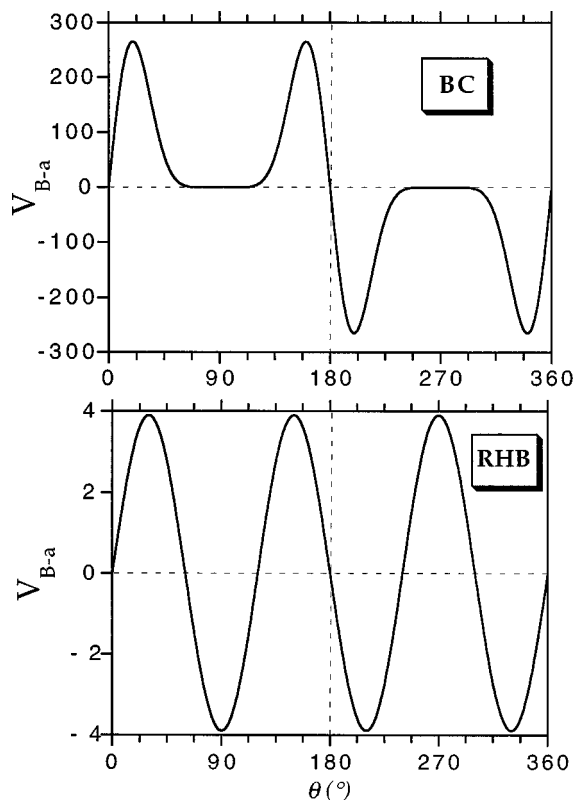


FIG. 14. Cuts of the off-diagonal surfaces coupling the  $B$  and the  $a$  potentials evaluated at  $5 \text{ \AA}$ . The BC curve is the DIM surface of Ref. 9, and RHB is the electrostatic surface of Ref. 12.

As before, the magnitude of the effective matrix element,  $|\langle V_{12} \rangle|$ , is obtained by summing over instantaneous solvent configurations and then taking the ensemble average. We evaluate Eqs. (18) and (19), under the assumption that the  $A$  coefficient is proportional to the polarizability of the solvent molecule. (Based on the value reported for Ar,<sup>12</sup> in the RHB model we use  $A = 3 \times 10^5$  and  $1.3 \times 10^6$  for Kr and  $CCl_4$ , respectively. In the BC form, based on the value given for Xe,<sup>9</sup> we use  $A = 2 \times 10^7$  and  $8.4 \times 10^7$  for Kr and  $CCl_4$ , respectively.)

The effect of solvent structure on solute predissociation probability can be gleaned from calculations of the effective matrix elements using static thermal distributions of the solvent. The results of these static calculations, using both isotropic and anisotropic  $I_2(X)$ -solvent potentials, are collected in Table III. Beside the difference in magnitudes, the table shows that the RHB and BC models make somewhat different predictions. Both models predict a reduction in coupling when using the isotropic potentials, an effect that can be traced to the reduction in local density. Despite the extensive cancellation due to local symmetry, due to the  $R^{-7}$  dependence, the RHB model predicts somewhat larger coupling in solid Kr than in liquid  $CCl_4$  for both the isotropic and anisotropic potentials. The BC model, for the anisotropic potential, predicts the liquid phase coupling magnitude to be a factor of 1.6 larger than the solid state, to be compared with the experimental value of 2.7. Within the statistical errors of the calculation, when using isotropic potentials, the BC

TABLE III. Predictions of effective electronic coupling ( $\text{cm}^{-1}$ ).

	Static, $ \langle V_{12} \rangle^e $			
	Anisotropic		Isotropic	
	Kr(s)	$CCl_4(l)$	Kr(s)	$CCl_4(l)$
RHB	8.5	5.9	5.9	5.2
BC	59	83	47	43
	Dynamic, $ \langle V_{12} \rangle^d $			
	490 nm		515 nm	580 nm
	Kr(s)	$CCl_4(l)$	$CCl_4(l)$	$CCl_4(l)$
	RHB	11	6.8	7.6
BC	39	108	109	82

model predicts nearly equal couplings for solid Kr and liquid  $CCl_4$ . The absolute magnitudes of the BC predictions are in surprisingly good agreement with experiment. The predicted solid state value of  $|\langle V_{12} \rangle^e| = 52 \text{ cm}^{-1}$  should be compared with the experimental value of  $65 \text{ cm}^{-1}$ , and the liquid phase value of  $82 \text{ cm}^{-1}$  is only a factor of 2 smaller than the experimental determination of  $175 \text{ cm}^{-1}$ .

Since the couplings are determined by asymmetry in the solvent structure, probabilities calculated based on static thermal distributions are expected to be quite different from those determined dynamically. In the latter case, the motion of the driven  $I_2$  oscillator will lead to cage distortions, the extent of which should depend on the initial preparation of the molecule. We carry out such calculations using the classical trajectories for 490, 515, and 580 nm preparations in liquid  $CCl_4$  (60 trajectories each). Now, the effective coupling is computed as an average over all crossings

$$|\langle V_{12} \rangle^d| = \frac{1}{N} \sum_j^N \sum_i V_{12}(r, \vartheta; t_j^*) \delta[\mathbf{r} - \mathbf{r}_i] \quad (20)$$

in which  $\mathbf{r}_i$  represent the instantaneous positions of the solvent atoms at the crossing time  $t^*$  (at  $R^* = 3.16 \text{ \AA}$ ), and the summation is over all  $N$  crossings of the swarm. The results are summarized in Table III.

The comparison of the 490 nm preparation shows that the RHB model predicts a larger coupling in the solid state, while now the BC model clearly predicts the liquid phase coupling to be larger by a factor of 2.7 almost identical to the ratio observed experimentally. Both models predict the dynamical effect observed experimentally, both show a larger coupling for preparation near the dissociation limit of the molecule (at 490 and 515 nm), in comparison to preparation deep in the bound part of the potential (at 580 nm). The BC model shows a  $\sim 30\%$  increase between 580 and 490 nm, which compares quite well with the energy dependence extracted from the experiment (inset to Fig. 13). As far as the absolute magnitudes are concerned, the BC predictions are in nearly quantitative agreement with experiment, the dynamical couplings being  $\sim 50\%$  of what is observed experimentally. Given the good agreement observed in our analysis, it is not clear to us why in the original simulations of BC extremely rapid predissociation was observed in solid Ar.<sup>9(b)</sup> We should perhaps re-emphasize that our analysis assumes

classical Landau–Zener, with a crossing fixed along the I–I coordinate, and a fixed gradient of the difference potential at the crossing point.

Independent of the detailed forms of the off-diagonal surface, the analysis clearly establishes the difference in predissociation probabilities between solid and liquid phases to be predominantly one of structure: Extensive cancellation of probability occurs in the highly symmetric solvent cage of the solid. Also, the simulations establish that indeed solute induced solvent fluctuations enhance the predissociation probabilities when large amplitude vibrations are set into motion. This effect was summarized in the experimental data using the modified LZ model, in terms of an electronic coupling that varies linearly with vibrational amplitude. In the case of the RHB model, we should note that, although the magnitude of the dipole–quadrupole interaction is too small to explain the observed predissociation rates, the mechanism is sound and should contribute to the overall rates. Moreover, in the case of  $I_2$ –Rg van der Waals complexes where the excited state is prepared in the ‘‘T’’-shaped geometry of the ground state, since the BC surface vanishes, the RHB coupling will dominate. This would explain the success of the RHB treatment of predissociation in the vdW complexes.<sup>12</sup>

## VI. CONCLUSIONS

Through ultrafast pump-probe measurements and theoretical analysis we have described the predissociation of  $I_2(B)$  in liquid  $CCl_4$ . The data is sensitive to a single crossing near  $v=0$ , and consistent with a nonadiabatic  $u \rightarrow g$  transition. This intramolecular electron transfer can be thought to occur via symmetry breaking of the solvent structure, and as such is sensitive to equilibrium distributions and dynamics of the first solvation shell. The seemingly surprising difference between liquid phase and solid state data can be explained by the difference in structural order in the two media and the dipolar coupling that drives the nonadiabatic dynamics in this case. That asymmetric cage vibrations induce such nonadiabatic transitions in highly symmetric isolation sites in rare gas matrices, has previously been noted in simulations.<sup>37</sup> The dynamical effect of symmetry breaking due to stirring of the liquid by the vibrationally excited molecule, leads to predissociation probabilities of  $\sim 1$  per period which are nearly independent of internal energy content in the molecule. This effect could be summarized in the experimental data by assuming an electronic coupling between surfaces that depends linearly on vibrational amplitude. The results are in nearly quantitative agreement with theory, when considering the DIM off-diagonal surface,  $V_{B-a}$ , recently provided by Batista and Coker.<sup>9</sup>

In addition to predissociation, the analysis provides important details of dynamics in the liquid phase. Vibrational relaxation and coherence are sensitive to solvent structure. The  $CCl_4$  data are consistent with a first solvation shell in which the distributions peak along the molecular axis. This in turn signifies an anisotropic  $I_2(X)$ – $CCl_4$  potential. The use of such a potential in simulations is able to reproduce the pump-probe transients, allowing a more detailed dissection

of the underlying dynamics with some confidence. In the anharmonic part of the potential, near the dissociation limit, upon the first collision with the solvent cage, the molecule undergoes a large energy transfer and complete scrambling of classical vibrational phases. The subsequent dynamics occurs in a relaxed cage, in the more harmonic region of the internal potential. The resulting biexponential energy decay is characterized by a  $\sim 100$  fs drop followed by a slow decay on a time scale  $\tau > 10$  ps. The latter decay process can not be well determined from the experiments, since predissociation occurs on a much shorter time scale. However, it is clear that when prepared deep in the  $B$  state potential, predissociation proceeds with complete retention of vibrational coherence. This picture was already evident in the studies by Scherer *et al.*, and our results are in general agreement with their observations and conclusions.<sup>5</sup>

Given the detailed understanding of electronic predissociation in this molecule, and the sensitivity of the process to solvent structure and dynamics, it can be used to characterize hosts in various media, such as supercritical fluids and glasses. Given our assessment of the DIM surfaces, it seems that through an iteration with experiments, a rather a complete description of the nonadiabatic dynamics of the full manifold of electronic states can be expected.

## ACKNOWLEDGMENTS

We gratefully acknowledge the support by AFOSR, under a University Research Initiative Grant No. F49620-1-0251, which made this work possible. We thank N. Halberstadt for stimulating discussions and for providing us with the derivation of the electrostatic model. We thank V. Batista and D. Coker for providing us the DIM points for the off-diagonal  $B-a$  surface. We acknowledge feedback given by M. Ben-Nun and R. Levine upon reading a preprint of this paper.

## APPENDIX

Given that the crossing between  $B(0_u^+)$  and  $a(1_g)$  surfaces has been identified as the most likely channel of predissociation, and the fact that in the experimental range of wavelengths, in particular at 490 and 515 nm a probe resonance between  $I^*I^*(1_u)$  and  $a(1_g)$  is expected, we consider the likely contribution of this probe window to the observed signal. To simulate signals arising from the final state of predissociation, we use trajectories propagated on the  $B$  potential to generate initial conditions for continuation on the  $a(1_g)$  surface. This is accomplished by storing the instantaneous positions and momenta of all particles for every time the trajectories reach the intersection between the two potentials, and subsequently continuing trajectories on the  $a(1_g)$  surface for an additional 250 fs. Thus a given trajectory on the  $B$  surface may spawn-off as many new trajectories as the number of times it passes the crossing point. These  $a(1_g)$  state trajectories are then given their appropriate LZ weights, and used for reconstructing the observable signal as before. Where contributions to the signal occur from both inside and outside the  $B$  surface, we recognize that transition dipole

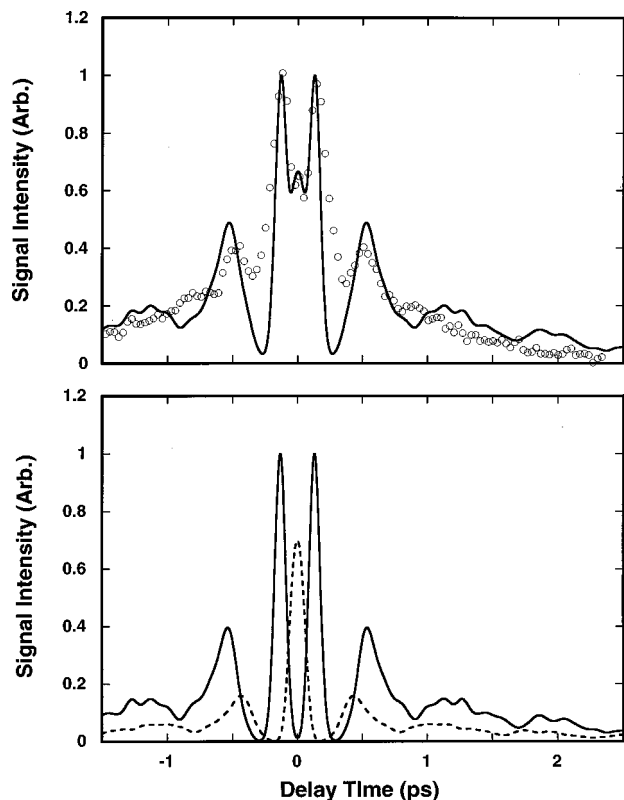


FIG. 15. Simulation of the 515 nm transient with one window located on each of the  $B$  and  $a(1_g)$  surfaces. The composition of the simulated signal is given in the lower panel: (dashed line)—contribution from  $B$  state; (solid line)—contribution from  $a(1_g)$  state. In the composite signal the  $a(1_g)$  state contribution is multiplied by 20.

moments need not be the same, and adjust the relative contributions to reproduce the experimental signal.

In Fig. 15 we show the best reproduction of the signal when we constrain the simulation to two windows, one on the  $B$  surface to reproduce the  $t=0$  peak, and one on the  $a(1_g)$  surface. A dissection of these contributions is also given in the figure. Since the predissociation probabilities are  $\sim 60\%$  per period, the net flux through each window is comparable, yet to obtain comparable intensities to the signal, it is necessary to assume a factor of 20 larger transition dipole for the resonance on the  $a(1_g)$  surface. This reduction in signal intensity is the result of the dramatically different velocities of the packets as they pass through the respective probe windows, due to the instantaneous kinetic energy of the packet during observation. There is no reason to expect the  $I^*I^*(1_u) \leftarrow a(1_g)$  transition to be stronger than the absorption from the  $B$  state. In fact, the opposite is true. At the large internuclear distances at issue, the  $I^*I^* \leftarrow I_2$  transition can be regarded as a two-electron transition, and should be significantly weaker than the  $E \leftarrow B$  charge transfer transition. Indeed, in the course of the spectroscopic studies on  $I^*I^*$  fluorescence spectra, we have searched and failed to see any emissions due to  $I^*I^* \rightarrow I_2$  transitions,<sup>16</sup> although a very

weak emission ascribed to this transition is observed in resonance Raman spectra in the solid state.<sup>38</sup> Thus, both due to the very weak transition strength, if at all detectable, and also due to the acceleration of trajectories on this surface, in the present experiments, the contribution of a probe signal from the  $a(1_g)$  surface is completely negligible.

- <sup>1</sup>T. J. Chuang, G. W. Hoffman, and K. B. Eisenthal, *Chem. Phys. Lett.* **25**, 201 (1974).
- <sup>2</sup>A. L. Harris, J. K. Brown, and C. B. Harris, *Ann. Rev. Phys. Chem.* **39**, 341 (1988).
- <sup>3</sup>T. J. Kang, J. Yu, and M. Berg, *J. Chem. Phys.* **94**, 2413 (1993).
- <sup>4</sup>D. E. Smith C. B. Harris, *J. Chem. Phys.* **87**, 2709 (1987).
- <sup>5</sup>N. F. Scherer, D. M. Jonas, and G. R. Fleming, *J. Chem. Phys.* **99**, 153 (1993).
- <sup>6</sup>R. Zadoyan, M. Sterling, and V. A. Apkarian, *J. Chem. Soc. Faraday Trans.* **92**, 1821 (1996).
- <sup>7</sup>C. Lienau, J. C. Williamson, and A. H. Zewail, *Chem. Phys. Lett.* **213**, 289 (1993); C. Lienau and A. H. Zewail, *ibid.* **222**, 224 (1994).
- <sup>8</sup>Q. Liu, C. Wan, and A. H. Zewail, *J. Chem. Phys.* **105**, 5294 (1996).
- <sup>9</sup>(a) V. S. Batista and D. F. Coker, *J. Chem. Phys.* **105**, 4033 (1996); (b) V. S. Batista and D. F. Coker, *J. Chem. Phys.* **106**, 7102 (1997).
- <sup>10</sup>A. A. Buchachenko and N. F. Stepanov, *J. Chem. Phys.* **104**, 9913 (1996).
- <sup>11</sup>M. Ben-Nun, R. D. Levine, and G. R. Fleming, *J. Chem. Phys.* **105**, 3035 (1996).
- <sup>12</sup>O. Roncero, N. Halberstadt, and J. A. Beswick, *J. Chem. Phys.* **104**, 7554 (1996).
- <sup>13</sup>C. Teichteil and M. Pelissier, *Chem. Phys.* **180**, 1 (1994).
- <sup>14</sup>R. M. Bowman, M. Dantus, and A. H. Zewail, *Chem. Phys. Lett.* **161**, 297 (1989).
- <sup>15</sup>R. S. Mulliken, *J. Chem. Phys.* **55**, 288 (1971).
- <sup>16</sup>A. Benderskii, R. Zadoyan, and V. A. Apkarian, *J. Chem. Phys.* **107**, 8437 (1997), preceding paper.
- <sup>17</sup>J. O. Hirschfelder, C. F. Curtiss, and R. B. Bird, *Molecular Theory of Gases and Liquids* (Wiley, New York, 1954).
- <sup>18</sup>C. H. Becker, P. Casavecchia, Y. T. Lee, R. E. Olson, and W. A. Lester, *J. Chem. Phys.* **70**, 5477 (1979).
- <sup>19</sup>B. E. Grigorenko, A. V. Nemukhin, and V. A. Apkarian, *Chem. Phys.* **219**, 161 (1997).
- <sup>20</sup>M. Ovchinnikov and V. A. Apkarian, *J. Chem. Phys.* **105**, 10312 (1996).
- <sup>21</sup>F. Yu. Naumkin and P. J. Knowles, *J. Chem. Phys.* **103**, 3392 (1995).
- <sup>22</sup>M. Sterling, R. Zadoyan, and V. A. Apkarian, *J. Chem. Phys.* **104**, 6497 (1996).
- <sup>23</sup>L. D. Landau and E. M. Lifshitz, *Quantum Mechanics* (Pergamon Press, Oxford, 1977); C. Zener, *Proc. R. Soc. London, Ser. A* **137**, 696 (1932).
- <sup>24</sup>L. Onsager, *J. Am. Chem. Soc.* **58**, 1486 (1936); R. Fulton, *J. Chem. Phys.* **61**, 4141 (1974).
- <sup>25</sup>J. C. D. Brand and A. R. Hoy, *Appl. Spectrosc. Rev.* **23**, 285 (1987).
- <sup>26</sup>J. Tellinghuisen, *J. Chem. Phys.* **76**, 4736 (1982).
- <sup>27</sup>Z. Li, R. Zadoyan, V. A. Apkarian, and C. C. Martens, *J. Phys. Chem.* **99**, 7453 (1995), and references therein.
- <sup>28</sup>J. Y. Fang and C. C. Martens, *J. Chem. Phys.* **105**, 9072 (1996).
- <sup>29</sup>J. S. Bader, B. J. Berne, E. Pollak, and P. Hanggi, *J. Chem. Phys.* **104**, 1111 (1996).
- <sup>30</sup>M. J. J. Vrakking, D. M. Villeneuve, and W. A. Stolow, *J. Chem. Phys.* **105**, 5647 (1996).
- <sup>31</sup>R. Zadoyan *et al.* (unpublished).
- <sup>32</sup>J. Xu, N. Schwentner, and M. Chergui, *J. Chem. Phys.* **101**, 7381 (1994); J. Xu, N. Schwentner, S. Hennig, and M. Chergui, *J. Chim. Phys.* **92**, 541 (1995); Xu, N. Schwentner, S. Hennig, and M. Chergui, *J. Raman Spectrosc.* **28**, 433 (1997).
- <sup>33</sup>M. Ovchinnikov and V. A. Apkarian, *J. Chem. Phys.* **106**, 5775 (1997).
- <sup>34</sup>C. A. Thayer and J. T. Yardley, *J. Chem. Phys.* **57**, 3992 (1972).
- <sup>35</sup>A. D. Buckingham, in *Intermolecular Forces*, edited by J. O. Hirschfelder (Interscience, New York, 1967).
- <sup>36</sup>N. Halberstadt (private communication).
- <sup>37</sup>K. Kizer, Ph.D. thesis, UCI, 1997.
- <sup>38</sup>A. I. Krylov, Ph.D. thesis, Hebrew University of Jerusalem, 1996.